The Astrophysical Journal, 893:101 (15pp), 2020 April 20 https://doi.org/10.3847/1538-4357/ab7cc8

An Unbiased ALMA Spectral Survey of the LkCa 15 and MWC 480 Protoplanetary Disks

Ryan A. Loomis[1], Karin I. Öberg[2], Sean M. Andrews[2], Edwin Bergin[3], Jennifer Bergner[2], Geoffrey A. Blake[4,5], L. Ilsedore Cleeves[6], Ian Czekala[7,11], Jane Huang[2], Romane Le Gal[2], Francois Ménard[8], Jamila Pegues[2], Chunhua Qi[2], Catherine Walsh[9], Jonathan P. Williams[10], and David J. Wilner[2]
[1] National Radio Astronomy Observatory, Charlottesville, VA 22903, USA; rloomis@cfa.harvard.edu
[2] Harvard-Smithsonian Center for Astrophysics, Cambridge, MA 02138, USA
[3] University of Michigan, Ann Arbor, MI 48109, USA
[4] Division of Chemistry and Chemical Engineering, California Institute of Technology, Pasadena, CA 91125, USA
[5] Division of Geological and Planetary Sciences, California Institute of Technology, Pasadena, CA 91125, USA
[6] Department of Astronomy, University of Virginia, Charlottesville, VA 22903, USA
[7] Department of Astronomy, 501 Campbell Hall, University of California, Berkeley, CA 94720-3411, USA
[8] Univ. Grenoble Alpes, CNRS, IPAG (UMR 5274) , F-38000 Grenoble, France
[9] School of Physics and Astronomy, University of Leeds, Leeds LS2 9JT, UK
[10] Institute for Astronomy, University of Hawai'i at Mānoa, Honolulu, HI 96822, USA
Received 2019 May 30; revised 2020 February 27; accepted 2020 March 3; published 2020 April 20

Abstract

The volatile contents of protoplanetary disks both set the potential for planetary chemistry and provide valuable probes of defining disk system characteristics such as stellar mass, gas mass, ionization, and temperature structure. Current disk molecular inventories are fragmented, however, giving an incomplete picture: unbiased spectral line surveys are needed to assess the volatile content. We present here an overview of such a survey of the protoplanetary disks around the Herbig Ae star MWC 480 and the T Tauri star LkCa 15 in ALMA Band 7, spanning ∼36 GHz from 275 to 317 GHz and representing an order of magnitude increase in sensitivity over previous single-dish surveys. We detect 14 molecular species (including isotopologues), with five species ($C^{34}S$, ^{13}CS, H_2CS, DNC, and C_2D) detected for the first time in protoplanetary disks. Significant differences are observed in the molecular inventories of MWC 480 and LkCa 15, and we discuss how these results may be interpreted in light of the different physical conditions of these two disk systems.

Unified Astronomy Thesaurus concepts: Protoplanetary disks (1300); Astrochemistry (75)

1. Introduction

Protoplanetary disks are the formation sites of planets, and their molecular inventories regulate the composition of nascent comets and planetesimals (e.g., Helling et al. 2014). These molecules also serve as valuable probes of disk properties such as stellar mass, temperature, and density gradients, ionization, and turbulence (e.g., Dutrey et al. 2007; Öberg et al. 2011; Rosenfeld et al. 2012, 2013; Cleeves et al. 2015; Czekala et al. 2015; Teague et al. 2016; Flaherty et al. 2018; Pinte et al. 2018). Disks are sufficiently cold, however, such that the a large fraction of the molecular content is locked up in ices in the disk midplane and unobservable with rotational spectroscopy. The resulting intrinsically low column densities have therefore limited the majority of disk observations thus far to targeted observations of specific molecules (e.g., Kastner et al. 2018), providing valuable insight for certain species, but still leaving incomplete inventories and a fragmented view of disk chemistry.

To date, 23 molecules (35 total species including isotopologues) have been discovered in disks, with the majority detected via rotational transitions (McGuire 2018). Expanding this molecular inventory is necessary to fully assess disk chemical compositions and develop new probes of chemistry and physics. First, many of the known species in disks have isotopologues which should be present but have not yet been detected, limiting our knowledge of processes such as nitrogen fractionation (e.g., Guzmán et al. 2017) and deuterium fractionation (e.g., Huang et al. 2017). Second, although small volatiles containing C/N/O have been well studied, S-bearing species have not yet been investigated in great detail, with studies of sulfur chemistry in disks limited mainly to CS and SO (e.g., Thi et al. 2004; Dutrey et al. 2007; Booth et al. 2018; Le Gal et al. 2019), and a recent detection of H_2S (Phuong et al. 2018). Thus, there are a number of potentially abundant S-bearing species that simply have not been searched for with deep integration times. Third, the recent detections of the complex organic molecules (COMs) CH_3CN, CH_3OH, and HCOOH in disks (Öberg et al. 2015; Walsh et al. 2016; Bergner et al. 2018; Favre et al. 2018; Loomis et al. 2018b) suggest that more complex species may be present. Indeed, disk chemistry models predict that a significant fraction of volatiles may be in the form of COMs as they form readily in irradiated ices (e.g., Bennett & Kaiser 2007; Garrod et al. 2008; Öberg et al. 2009), and the ramifications of the resultant chemical CO depletion are extremely important to characterize when considering disk masses (e.g., Miotello et al. 2016, 2017; Yu et al. 2017) and C/O ratios (e.g., Schwarz et al. 2018).

Unbiased spectral line surveys offer the potential to fill these gaps. Historically used as a powerful tool to probe the molecular inventories of cold clouds and star-forming regions (e.g., Johansson et al. 1984; Blake et al. 1986, 1994; van Dishoeck et al. 1995; Kaifu et al. 2004; Belloche et al. 2008a; Remijan et al. 2009), single-dish surveys have also expanded our understanding of molecular complexity through a large number of serendipitous molecular detections

[11] NASA Hubble Fellowship Program Sagan Fellow.

Table 1
Disk Properties

Source	Stellar Type	R.A.[a] (J2000)	Decl.[a] (J2000)	Dist.[a] (pc)	$L_\star$ ($L_\odot$)	$M_\star$ ($M_\odot$)	Disk Mass ($M_\odot$)	Incl. (deg)	P.A. (deg)	Age (Myr)	V_{LSRK} (km s^{-1})
MWC 480	A1–A3/4 (1, 2)	04:58:46.3	29:50:37.0	162	19–24 (3, 4)	1.7–2.3 (3, 4, 5)	0.11 (6)	37 (7)	148 (7)	6–7.1 (3, 4, 5)	5.1 (7)
LkCa 15	K3–K5 (2, 8)	04:39:17.8	22:21:03.4	159	0.8 (3)	1.0 (3,5)	0.05–0.1 (9)	52 (7)	60 (7)	3–5 (3, 5, 10)	6.3 (7)

Note.
[a] R.A., decl., and distance of each source are from the Gaia DR2 catalog (Gaia Collaboration et al. 2018).
References. [1] The et al. (1994), [2] Luhman et al. (2010), [3] Andrews et al. (2013), [4] Mannings & Sargent (1997), [5] Simon et al. (2000), [6] Chiang et al. (2001), [7] Huang et al. (2017), [8] Herbig & Bell (1988), [9] Isella et al. (2012), [10] Guilloteau et al. (2014).

Table 2
Observation Details

Setting[a]	Date	Antennas[b]	Baselines (m)	On-source int. (minutes)[c]	Bandpass Cal.	Phase Cal.	Flux Cal.
A	2016 Jan 17	36	15–331	19.2	J0510+1800	J0438+3004	J0510+1800
B	2016 Jan 17	31	15–331	17.6	J0510+1800	J0438+3004	J0510+1800
	2016 Apr 23	36	15–463	12.6	J0238+1636	J0433+2905	J0510+1800
	2016 Dec 12	36	15–650	20.7	J0510+1800	J0438+3004	J0510+1800
C	2016 Dec 13	39	15–650	20.2	J0510+1800	J0438+3004	J0510+1800
D	2016 Dec 13	36	15–650	12.6	J0510+1800	J0438+3004	J0510+1800
	2016 Dec 14	39	15–460	12.6	J0510+1800	J0438+3004	J0510+1800
E	2016 Dec 17	40	15–460	13.1	J0510+1800	J0438+3004	J0510+1800
	2016 Dec 18	42	15–492	13.1	J0510+1800	J0438+3004	J0510+1800

Notes.
[a] See Table 3 for details on each spectral setting.
[b] Number of antennas remaining after flagging.
[c] Single source integration time. MWC 480 and LkCa 15 had equal integration times for all observations.

(e.g., Belloche et al. 2008b, 2009; Ossenkopf et al. 2010; McGuire et al. 2012, 2016; Pety et al. 2012; Loomis et al. 2013; Zaleski et al. 2013). Recent advances in sensitivity have additionally allowed similar single-dish survey exploration of disks (e.g., Kastner et al. 2014; Punzi et al. 2015). With the construction of the Atacama Large Millimeter/submillimeter Array (ALMA), these sensitive line surveys can now be conducted efficiently (∼20 minutes on-source integration per source per setting) with simultaneous high resolution imaging (e.g., Jørgensen et al. 2016; Belloche et al. 2017), providing a clear opportunity for unbiased interferometric line surveys of disks.

We have undertaken a spectral line survey of the protoplanetary disks around MWC 480 and LkCa 15 in ALMA Band 7, spanning ∼36 GHz from 275 to 317 GHz and representing an order of magnitude improvement in sensitivity compared with previous single-dish surveys of disks (e.g., Kastner et al. 2014; Punzi et al. 2015). Both MWC 480, a Herbig Ae star, and LkCa 15, a T Tauri star, reside in the nearby Taurus star-forming region (∼160 pc Gaia Collaboration et al. 2018). They are both relatively young (∼3–7 Myr) and host large (>200 au) well-studied gas-rich disks (e.g., Chiang et al. 2001; Piétu et al. 2007; Öberg et al. 2011; Isella et al. 2012; Huang et al. 2017). Differences in the luminosity, disk mass, and temperature between these two sources (see Table 1) allow for a preliminary investigation of the effect these parameters play in setting the disk molecular inventory.

In this paper, we present an overview of the line survey and summarize the molecular content of both disks. We find evidence for 14 molecular species in total (including isotopologues), with five species detected in a protoplanetary disk for the first time. We present the details of the observations and the data calibration in Section 2. In Section 3, we describe our data analysis methods, in which the survey is imaged in an unbiased manner and a matched filtering technique is used to efficiently identify lines. Section 4 then presents an overview of the imaged data, as well as images and spectra for each molecular detection. In Section 5, we compare the molecular inventory of the two sources and discuss how their physical characteristics may relate to the observed chemical differences. We additionally briefly discuss the low degree of chemical complexity observed in the context of predictions from chemical models. A summary is given in Section 6.

2. Observations

LkCa 15 and MWC 480 were observed in Band 7 during ALMA Cycles 3 and 4 (project code 2015.1.00657.S). Six correlator setups were designed to provide nearly complete frequency coverage between 275 and 322 GHz. Each spectral setup consisted of 4 Frequency Division Mode spectral windows, each with 1920 channels. The channel width was 975 kHz, resulting in a velocity resolution of ∼1 km s^{-1}. Only the first five of these setups had observations taken, resulting in coverage gaps between 306–310 GHz and 318–322 GHz. Observational details including number of antennas, uv-coverage, on-source integration time, and calibrator information are listed in Table 2. Details of the spectral setups are listed in Table 3.

Data was initially calibrated by the ALMA/NAASC staff. Subsequent self-calibration and imaging of the data were completed using `CASA` 4.3.1. For each execution and disk, the dust continuum was imaged by `CLEAN`ing the line-free

Table 3
Details of Spectral Settings

Setting	SPW	Frequencies (GHz)	Beam (PA)		Per chan. rms (mJy bm^{-1})	
			MWC 480	LkCa 15	MWC 480	LkCa 15
A	0	275.20–277.08	1.″30 × 1.″05 (12.°7)	1.″18 × 1.″04 (−42.°9)	2.7	2.8
	1	277.08–278.95	1.″27 × 1.″03 (12.°6)	1.″15 × 1.″02 (−43.°3)	3.0	3.1
	2	287.20–289.08	1.″22 × 1.″00 (−9.°7)	1.″11 × 0.″99 (−44.°6)	3.3	3.4
	3	289.08–290.95	1.″22 × 1.″01 (168.°9)	1.″10 × 0.″97 (−45.°7)	3.3	3.4
B	0	278.95–280.83	1.″13 × 0.″60 (−30.°6)	1.″03 × 0.″60 (−38.°4)	1.8	1.7
	1	280.82–282.70	1.″12 × 0.″59 (−30.°4)	1.″02 × 0.″60 (−38.°0)	1.9	1.8
	2	290.95–292.83	1.″10 × 0.″60 (−32.°5)	0.″98 × 0.″58 (−38.°2)	2.2	2.2
	3	292.82–294.70	1.″07 × 0.″57 (149.°5)	0.″98 × 0.″58 (−38.°3)	2.0	2.0
C	0	283.45–285.33	0.″99 × 0.″53 (−177.°5)	0.″85 × 0.″53 (177.°3)	2.3	2.3
	1	285.33–287.20	0.″99 × 0.″53 (175.°8)	0.″85 × 0.″53 (−2.°9)	2.5	2.6
	2	295.45–297.33	0.″95 × 0.″52 (−4.°4)	0.″83 × 0.″52 (170.°5)	2.6	2.6
	3	297.33–299.20	0.″94 × 0.″51 (−3.°9)	0.″83 × 0.″52 (171.°3)	2.5	2.5
D	0	298.30–300.18	1.″00 × 0.″56 (−25.°4)	0.″91 × 0.″55 (−33.°8)	3.0	3.1
	1	300.18–302.06	1.″04 × 0.″58 (−30.°0)	0.″96 × 0.″56 (141.°0)	3.4	3.6
	2	310.30–312.18	1.″00 × 0.″56 (−29.°7)	0.″92 × 0.″55 (141.°2)	3.5	3.7
	3	312.18–314.06	0.″95 × 0.″53 (155.°2)	0.″86 × 0.″53 (−33.°2)	3.7	3.9
E	0	302.05–303.93	0.″94 × 0.″62 (179.°2)	0.″82 × 0.″63 (−8.°2)	2.0	2.0
	1	303.93–305.81	0.″94 × 0.″62 (179.°0)	0.″82 × 0.″63 (−8.°4)	2.1	2.1
	2	314.05–315.93	0.″91 × 0.″60 (179.°2)	0.″79 × 0.″61 (171.°9)	2.5	2.4
	3	315.93–317.81	0.″90 × 0.″60 (178.°8)	0.″79 × 0.″61 (171.°2)	2.9	2.9

portions of the data with a Briggs robust parameter of −0.5. Three rounds of phase-only self-calibration on the disk continuum emission were then completed with solution intervals of 100 s, 30 s, and 10 s, followed by one iteration of amplitude self-calibration. These calibration tables were applied to the full data for each execution, and the individual spectral windows were then split and continuum subtracted using the CASA task `uvcontsub` (fit-order = 1).

3. Data Analysis

3.1. Initial Full-band Imaging and Spectral Extraction

Each of the spectral windows for both sources was imaged with `CLEAN` in CASA 4.3.1, using natural weighting for optimal sensitivity. Resultant synthesized beam sizes and position angles for each spectral window are listed in Table 3. When a spectral setting had multiple executions taken, the respective measurement sets for each spectral window were concatenated prior to imaging. Each window was initially dirty imaged to determine a characteristic per-channel rms, listed in Table 3. They were then `CLEAN`ed down to a threshold of 4σ, with elliptical `CLEAN` masks defined for each source to contain the full extent of the gas disk. For MWC 480, the mask had a major axis length of 3.″5, inclination of 37°, and PA of 148° (Chiang et al. 2001; Piétu et al. 2007; Öberg et al. 2011). For LkCa 15, the mask had a major axis length of 4.″5, inclination of 52°, and PA of 60° (Piétu et al. 2007; Isella et al. 2012). These elliptical masks were applied uniformly across all channels to preserve the unbiased nature of the survey. After imaging, disk-integrated spectra were extracted from the image cubes using the elliptical `CLEAN` masks. The spectra were averaged where spectral window 3 from setting C and spectral window 0 from setting D overlap.

The full extracted spectra of MWC 480 and LkCa 15 are shown in Figure 1 in blue and mirrored in red, respectively. Lines visible in the spectra are labeled in the figure, with the location of the label above/below the baseline denoting in which disk the line is stronger. Sections of the spectrum where atmospheric absorption lines are present are plotted with transparency, and the somewhat different sensitivity of each spectral window is visible in the figure.

3.2. Matched Filtering

The data were further analyzed by applying a bank of matched filters to attempt to locate any additional weak lines. When the shape of a signal is known (or can be well-approximated), application of a matched filter allows for maximal signal extraction (North 1963). In Loomis et al. (2018c), we developed a method to efficiently apply matched filters to interferometric observations, allowing the quick analysis of high bandwidth interferometric spectral surveys and an improved signal-to-noise ratio (S/N). Previous observations of both MWC 480 and LkCa 15 (e.g., Öberg et al. 2010, 2011; Huang et al. 2017) have determined the Keplerian rotation pattern of both disks, as well as a variety of radial emission profiles for different molecular species. We use prior observations of ^{12}CO, ^{13}CO, C^{18}O, DCO$^+$, and H^{13}CO$^+$ (Huang et al. 2017) to generate a bank of data-driven template filters to apply to the line survey data. Filters were also created using strong lines of H_2CO, N_2H^+, and CS imaged from the presently described observations. All of these filters describe identical Keplerian rotation patterns, and thus will likely yield similar results for a given target line, but small differences between the filter responses may provide useful clues about the target line emission morphology, especially if the target line is too weak to image at high resolution. Moment-0 integrated emission maps of each of the filter template molecules are shown in Figure 2, demonstrating the broad range of emission patterns.

Each of the template transitions were imaged with `CLEAN`, and relatively noise-free approximations of the emission were created by convolving the `CLEAN` components with their respective restoring beams. These image cubes were then used as data-driven filters and applied to each continuum-subtracted

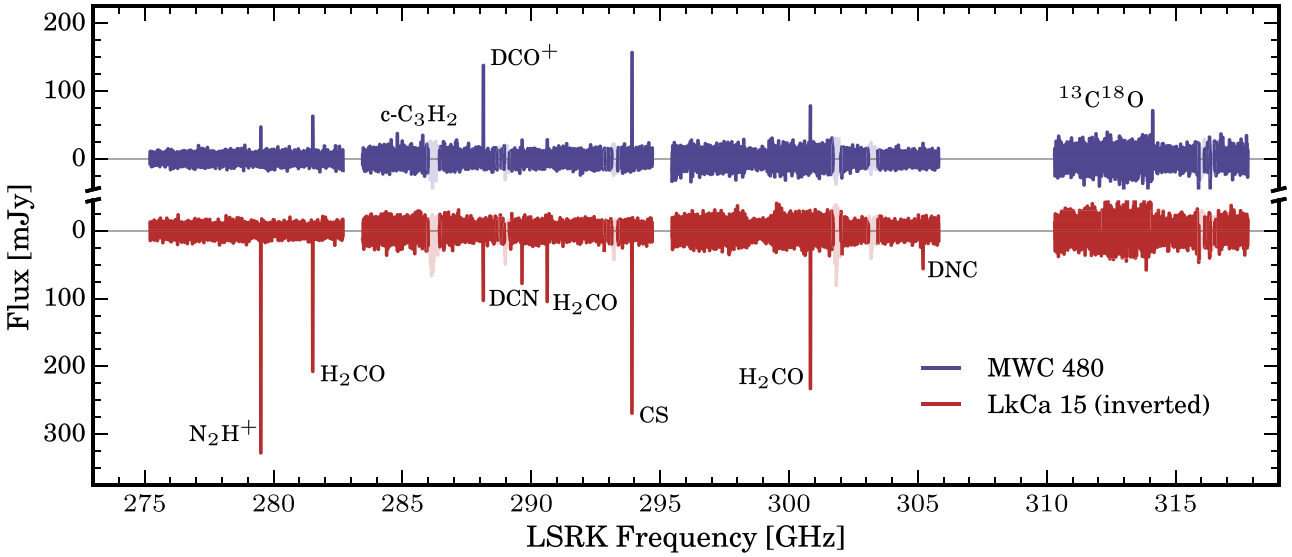

Figure 1. Spectra extracted with the elliptical CLEAN masks for each disk. The spectrum of MWC 480 is shown in blue and that of LkCa 15 is mirrored in red, with spectral regions contaminated by atmospheric absorption lines plotted with transparency. Molecular species with transitions detected at a 4σ level are labeled, with the label location denoting within which disk the species is more strongly detected.

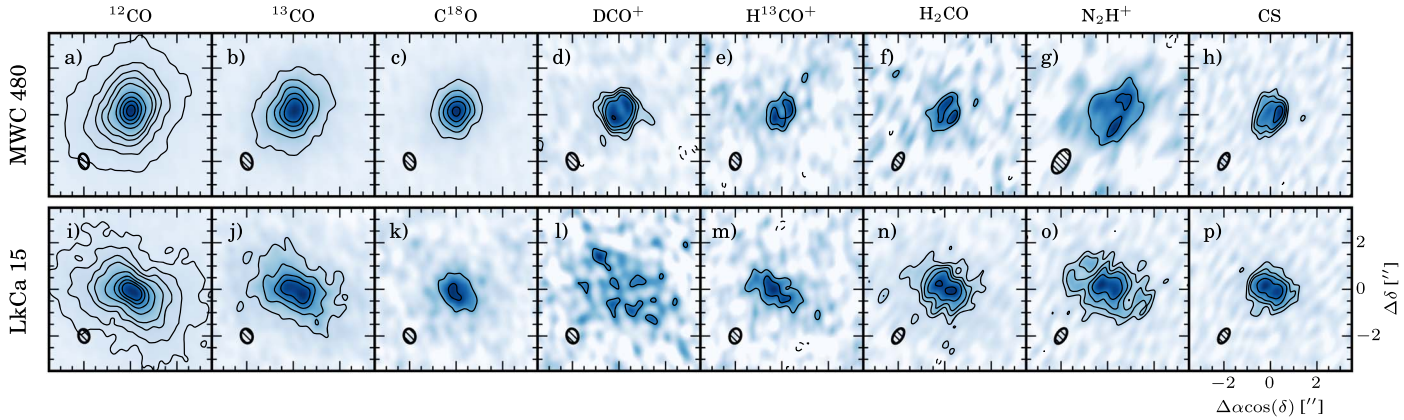

Figure 2. Moment-0 integrated emission maps of observations used as matched filter templates, demonstrating varied emission morphology. Emission for all species has been normalized by dividing by the peak emission. Contours for MWC 480 CO isotopologues (panels a–c) are [10, 20, 30, 40, 50, 75, 100, 125, 150] $\times$ σ and contours for LkCa CO isotopologues (panels i–k) are [5, 10, 15, 20, 30, 40, …] $\times$ σ. Contours for all other panels are [3, 5, 7, 10, 15, 20, …] $\times$ σ. Synthesized beams are shown in the lower left of each panel.

spectral window using the VISIBLE package (Loomis et al. 2018a).[12] As the image cubes do not all match the native velocity resolution of our observations, VISIBLE interpolates the filters to match the local velocity resolution of the data being filtered. The interpolated filter is then convolved with the data, producing a normalized filter impulse response spectrum. The technical details of this method can be found in Loomis et al. (2018c). Spectra from spectral windows that contained multiple executions were first combined via a weighted average, with weights calculated from the rms in each response spectrum, and then normalized after averaging.

The full survey filter impulse response spectrum for the $H^{13}CO^+$ template is shown in Figure 3 as an illustrative example. Response spectra for the other filter templates produced similar results and are available online as a figure set. The spectrum of MWC 480 is shown in blue and that of LkCa 15 is mirrored in red. As in Figure 1, regions contaminated by atmospheric features are plotted with transparency. A comparison with Figure 1 demonstrates that application of a matched filter results in a higher S/N spectrum. and many weak lines that were previously not seen in Figure 1 are now visible. Observed lines of the detected species are labeled in the figure, with the location of the label above/below the baseline denoting within which disk the species is more strongly detected. At any given frequency, the sensitivity of both the MWC 480 and LkCa 15 spectra are nearly identical (given the identical integration times, similar uv-coverage, similar angular sizes of the disks, and similar linewidths), so a comparison of filter responses between the two disks likely reflects emission strength differences between them. Due to the varied execution time and weather conditions of each setting, however, the individual spectral windows do not have uniform sensitivity and thus we stress that the full normalized spectrum does not portray individual line emission intensity (i.e., the ratio of filter responses of lines in different spectral windows does not reflect the ratio of their total integrated emission). This is especially clear in the relative filter responses of the three

[12] VISIBLE is publicly available under the MIT license at https://github.com/AstroChem/VISIBLE or in the Anaconda Cloud at https://anaconda.org/rloomis/VISIBLE.

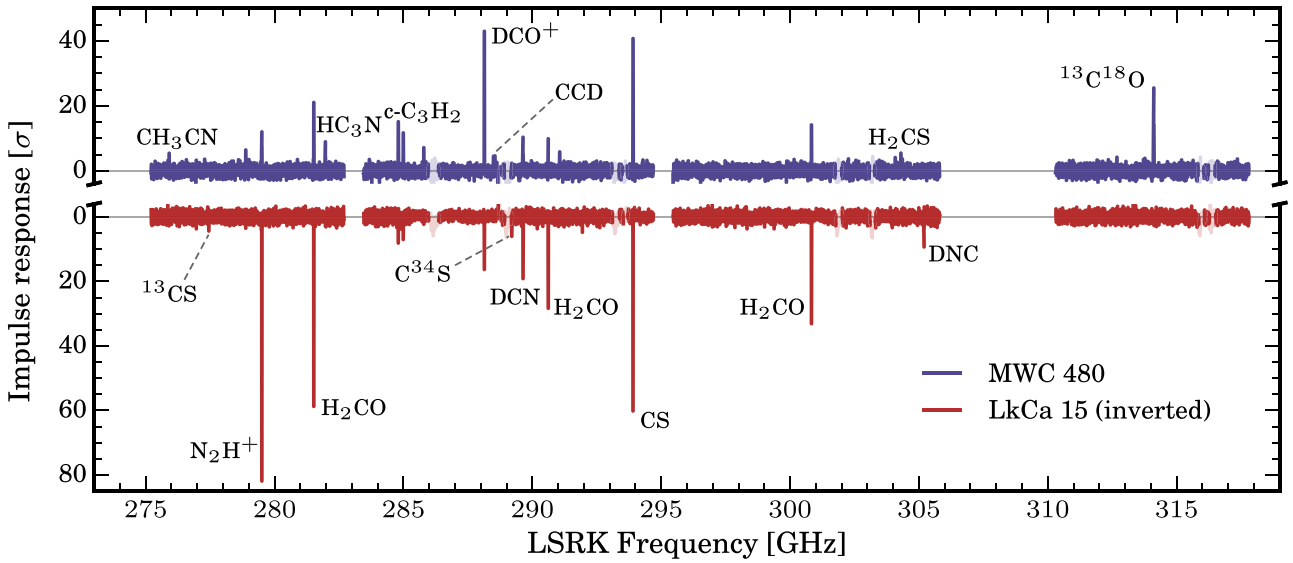

Figure 3. Impulse response spectra for the entire observed bandwidth, produced by filtering the observations with the $H^{13}CO^+$ template kernel. The spectrum of MWC 480 is shown in blue and that of LkCa 15 is mirrored in red, with spectral regions contaminated by atmospheric absorption lines plotted with transparency. Molecular species with transitions detected at a 4σ level are labeled, with the label location denoting in which disk the species is more strongly detected.

strong H_2CO lines in LkCa 15: the 4_{14}–3_{13} transition at 281.5 GHz and the 4_{13}–3_{12} transition at 300.8 GHz have very similar integrated emission, but different filter responses, as the 4_{13}–3_{12} transition is in a noisier spectral window. This note aside, the filter response spectra allow for quick identification of all lines detected in the survey.

3.3. Individual Line Imaging and Flux Measurement

All spectral lines that were detected by matched filtering in either disk at greater than 4σ significance were then individually imaged with CLEAN using natural weighting. Lines that were strongly detected ($>20\sigma$) were imaged at higher spatial resolution. An identical imaging process was used, but with Briggs weighting and a robust value of 0.5. Lower values of robustness produced images with substantially higher noise and thus were not used. The resultant synthesized beam parameters are listed in the respective figure captions in Section 4. Velocity mode in CLEAN was used with a channel width of 1.5 km s^{-1}, so that all lines would be on a regular velocity grid. The previously described elliptical CLEAN masks were used for each disk, and the image cubes were CLEANed down to a threshold of 4σ, using the rms values listed in Table 3. Disk-integrated spectra were then extracted from the image cubes using the CLEAN masks. Fluxes for each transition were determined by integrating these spectra from 2.0 to 9.5 km s^{-1} and 3.5 to 11 km s^{-1} in MWC 480 and LkCa 15, respectively, and are listed in Table 4. Uncertainties on each flux measurement were determined through bootstrapping, repeating this process 10,000 times on randomly selected nearby emission-free channels, sampled with replacement (see, e.g., Bergner et al. 2018, for a description of this technique). The standard deviations of these values are reported as the uncertainty on the flux measurements.

4. Results

4.1. Overview

As shown in Figures 1 and 3, we detect 14 molecular species (including isotopologue s) at a $>4\sigma$ significance toward MWC 480 and LkCa 15, with five of these species ($C^{34}S$, ^{13}CS, H_2CS, DNC, and C_2D) detected for the first time in a protoplanetary disk (as also presented in Le Gal et al. (2019) for the S-bearing species). Eleven species were detected toward MWC 480, with DNC, $C^{34}S$, and ^{13}CS not detected, and nine species detected toward LkCa 15, with $^{13}C^{18}O$, H_2CS, C_2D, HC_3N, and CH_3CN not detected. Observed transitions of the 14 detected species are tabulated in Table 4. Integrated fluxes (or 2σ upper limits for lines not detected at $>4\sigma$ with any filter) are listed for each transition, extracted as described in Section 3.1. The filters that yielded the strongest impulse response for each transition are listed, along with the respective significance of the response (self-filtered responses for the strong lines of H_2CO, N_2H^+, and CS were excluded). From both the above figures and Table 4, it is clear that the molecular inventories of MWC 480 and LkCa 15 differ dramatically, which might be expected given their different stellar masses, disk masses, radiation environments, and average temperatures. Emission morphologies and their differences are explored on a per molecule basis in the following sub-sections, and then discussed further in Section 5.

4.2. CO Isotopologues: $^{13}C^{18}O$

Figure 4 shows that $^{13}C^{18}O$ 3–2 emission is strongly detected ($>20\sigma$) in MWC 480 but not observed in LkCa 15. The emission in MWC 480 is compact and centrally peaked, similar to the $C^{18}O$ emission shown in Figure 2. If $^{13}C^{18}O$ is optically thin, its radial extent may directly trace the CO snowline (e.g., Zhang et al. 2017). By deprojecting and azimuthally averaging the emission and then deconvolving the beam, we find that the emission extends out to ~120 au. This is roughly in agreement with predictions from the temperature profile used in Öberg et al. (2015), where a 20 K snowline would be at ~135 au. A more detailed investigation of the midplane temperature profile of MWC 480 is beyond the scope of this paper, but the high S/N of the $^{13}C^{18}O$ detection suggest that an analysis of the CO isotopologues similar to that presented in Zhang et al. (2017) is feasible for MWC 480.

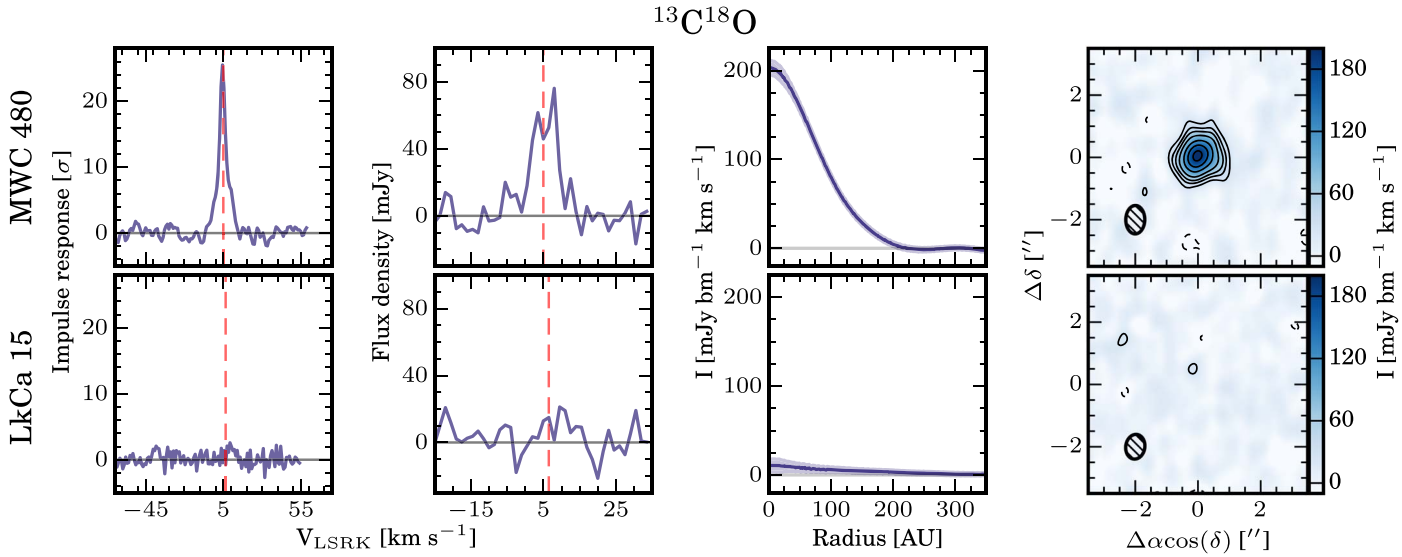

Figure 4. $^{13}C^{18}O$ observations in MWC 480 (top) and LkCa 15 (bottom). Far left: matched filter impulse response spectra using the filter which yielded the strongest response (see Table 3). Source systemic velocity is denoted by the dashed red line. Middle left: aperture-extracted spectra. Source systemic velocity is denoted by the dashed red line. Middle right: deprojected and azimuthally averaged radial profiles. 1σ uncertanties are shown in shaded blue. Far right: moment-0 maps showing total integrated $^{13}C^{18}O$ emission. All contours are [−3, 3, 5, 7, 10, 15, 20, 25, …] × σ.

Table 4
Observed Spectral Lines

Species	Transition	Frequency (MHz)	E_u (K)	$S_{ij}\mu^2$ (D^2)	MWC 480 Integrated Flux Density (mJy km s^{-1})	MWC 480 Filter Response (σ)	MWC 480 Filter	LkCa 15 Integrated Flux Density (mJy km s^{-1})	LkCa 15 Filter Response (σ)	LkCa 15 Filter
$^{13}C^{18}O$	3–2	314199.7[a]	30.2	0.073[b]	422 ± 34	25.5	CS	79 ± 31	…[c]	…[c]
N_2H^+	3–2	279511.7	26.8	335.2	228 ± 13	17.7	$C^{18}O$	1750 ± 20	89.8	$C^{18}O$
H_2CO	4_{04}–3_{03}	290623.4	34.9	21.7	153 ± 18	12.8	N_2H^+	581 ± 25	34.4	$C^{18}O$
	4_{14}–3_{13}	281526.9	45.6	61.1	324 ± 19	23.6	N_2H^+	1152 ± 19	71.5	^{13}CO
	4_{13}–3_{12}	300836.6	47.9	47.9	342 ± 22	16.4	$C^{18}O$	1334 ± 34	39.4	$C^{18}O$
	4_{22}–3_{21}	291948.1	82.1	16.3	<60[d]	…[c]	…[c]	80 ± 30	4.0	$C^{18}O$
DCO^+	4–3	288143.9[a]	34.6	189.3[b]	784 ± 16	46.4	H_2CO	502 ± 17	26.7	^{13}CO
DCN	4–3	289645.2[a]	34.8	114.7[b]	104 ± 19	10.3	CS	410 ± 22	23.6	N_2H^+
DNC	4–3	305206.2[a]	36.6	37.2[b]	<32[d]	3.6	$H^{13}CO^+$	228 ± 22	15.9	^{13}CO
CS	6–5	293912.1	49.4	22.9	811 ± 19	41.0	DCO^+	1497 ± 19	62.9	H_2CO
$C^{34}S$	6–5	289209.1	38.2	22.2	<32[d]	…[c]	…[c]	90 ± 19	6.2	H_2CO
^{13}CS	6–5	277455.4	46.6	23.0	<28[d]	…[c]	…[c]	61 ± 17	4.4	H_2CO
H_2CS	8_{17}–7_{16}	278886.4	73.4	64.1	83 ± 19	6.4	CS	<40[d]	3.5	CS
	9_{19}–8_{18}	304306.0	86.2	72.3	51 ± 18	5.4	CS	<38[d]	…[c]	…[c]
	9_{18}–8_{17}	313714.9	88.5	72.3	80 ± 41	4.2	$H^{13}CO^+$	52 ± 45	4.2	$H^{13}CO^+$
c-C_3H_2	8_{18}–7_{07}	284805.2[e]	64.3	239.2	166 ± 23	15.1	CS	104 ± 32	8.1	CS
	7_{16}–6_{25}	284998.0[f]	61.2	174.0	143 ± 21	11.7	CS	101 ± 28	7.0	CS
	6_{34}–5_{23}	285795.7	54.7	110.8	118 ± 24	7.3	$H^{13}CO^+$	<68[d]	…[c]	…[c]
C_2D	4–3 $J=\frac{9}{2}-\frac{7}{2}$	288499.0[a]	34.6	7.6[b]	63 ± 22	4.5	DCO^+	<44[d]	…[c]	…[c]
	4–3 $J=\frac{7}{2}-\frac{5}{2}$	288554.6[a]	34.6	5.7[b]	84 ± 16	4.9	DCO^+	<40[d]	…[c]	…[c]
HC_3N	31–30	281976.8[a]	216.5	431.7[b]	107 ± 16	8.9	CS	44 ± 18	…[c]	…[c]
	32-31	291068.4[a]	230.5	445.6[b]	85 ± 19	5.8	CS	64 ± 21	…[c]	…[c]
	33-32	300159.7[a]	244.9	459.6[b]	102 ± 22	3.6	DCO^+	<56[d]	…[c]	…[c]
CH_3CN	15_0–14_0	275915.6[a]	105.9	1700[b]	60 ± 20	5.4	CS	<32[d]	…[c]	…[c]
	16_0–15_0	294302.4[a]	120.1	1814[b]	50 ± 10	3.2	CS	<38[d]	…[c]	…[c]

Notes.
[a] Center frequency of collapsed hyperfine components (spacing smaller than channel width).
[b] $S_{ij}\mu^2$ of combined hyperfine components.
[c] …denotes transition not detected above 3σ with any filter.
[d] Upper limits are 2σ.
[e] c-C_3H_2 8_{18}–7_{07} is spectrally coincident with c-C_3H_2 8_{08}–7_{17}.
[f] c-C_3H_2 7_{16}–6_{25} is partially blended with c-C_3H_2 7_{26}–6_{15}.

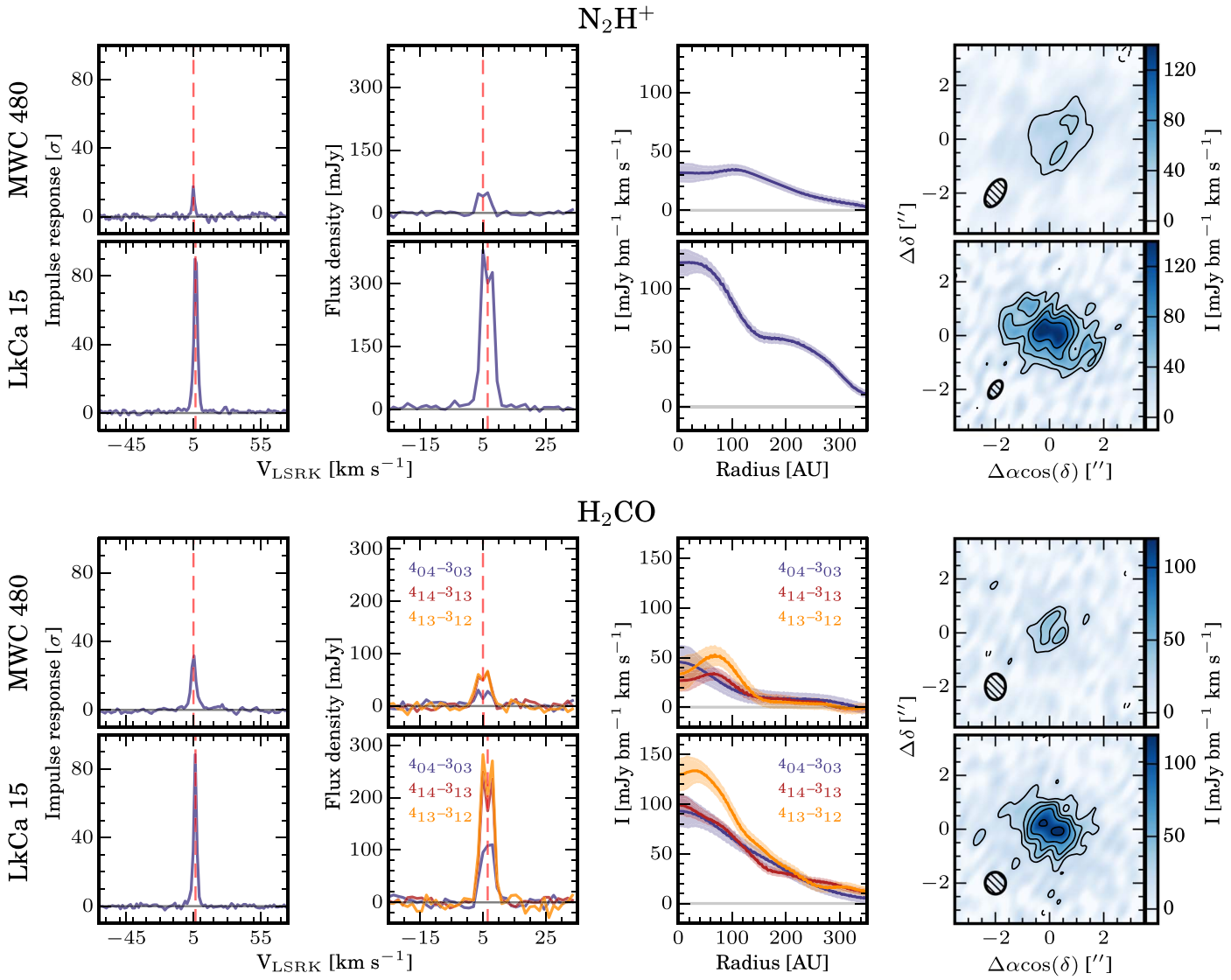

Figure 5. N_2H^+ (top) and H_2CO (bottom) observations in MWC 480 and LkCa 15. Panel descriptions are identical to Figure 4. The H_2CO impulse response and moment-0 panels show stacked data, while the aperture-extracted spectra and radial profiles are shown for each individual transition. The same convention is used for all subsequent figures.

4.3. Species Sensitive to CO Freeze-out: N_2H^+ and H_2CO

N_2H^+ 3–2 emission is strongly detected toward both disks (Figure 5), but is much brighter toward LkCa 15 (flux ratio of ∼7.7; 1750 ± 20 versus 228 ± 13 mJy km s^{-1}, respectively). Without detailed chemical modeling, it is unclear whether this is due to effects such as variations in total elemental abundances or ionization between the disks, or enhanced destruction in MWC 480 due to a higher disk temperature and less CO freeze-out. Similar to $^{13}C^{18}O$, N_2H^+ has also been proposed as a tracer of the CO snowline (e.g., Qi et al. 2013a, 2013b, 2015), although its simplicity as a tracer of the snowline location has been debated (van't Hoff et al. 2017). Reaction with CO is one of the main destruction pathways of N_2H^+, and the inner edge of its emission ring may therefore trace the midplane CO abundance profile. The N_2H^+ emission in both disks demonstrate this ringed morphology, although the emission around LkCa 15 displays a double ring. A similar double-ring morphology has been observed for both DCN and $H^{13}CO^+$ in LkCa 15 (Huang et al. 2017). By deprojecting and azimuthally averaging the emission from both disks, we find an inner ring radius of ∼115 au for MWC 480 and ∼40 au for LkCa 15. The second ring of emission in LkCa 15 peaks at ∼220 au. The N_2H^+ inner ring radius for MWC 480 is similar to the radial edge of the $^{13}C^{18}O$ emission, supporting the hypothesis that they are both tracing the CO snowline location.

Multiple lines of H_2CO are strongly detected toward both disks (Figure 5), but as with N_2H^+ the emission is much brighter toward LkCa 15 (flux ratios of 3.5–3.9). Grain surface formation of H_2CO through sequential hydrogenation of CO is thought to be a major contributor to H_2CO abundances in disks (Watanabe & Kouchi 2002; Fuchs et al. 2009; Qi et al. 2013a; Loomis et al. 2015; Carney et al. 2017; Öberg et al. 2017). Similar logic may hold as with N_2H^+ then, where CO freeze-out in the colder LkCa 15 disk enhances H_2CO formation compared with the warmer MWC 480 disk. The H_2CO in LkCa 15 also has an emission profile that is suggestive of a possible double ring, similar to that seen for N_2H^+. The detection of many lines of H_2CO spanning a wide range of upper state energies (35–82 K) enables the use of rotational diagrams to constrain the H_2CO excitation temperature (e.g.,

Carney et al. 2017), and further analysis of these observations are presented within the context of a larger survey of H_2CO in protoplanetary disks in Pegues et al. (2020).

4.4. Deuterated Species: DCO^+, DCN, and DNC

An inventory of the deuterium chemistry of a small sample of protoplanetary disks, including both MWC 480 and LkCa 15, was initially explored in Huang et al. (2017), tracing the $J = 3$–2 transitions of both DCO^+ and DCN, as well as their ^{13}C isotopologues. Here we observe the $J = 4$–3 transitions of these species and find very similar results. As in Huang et al. (2017), we observe bright compact emission of DCO^+ in MWC 480 and more diffuse emission in LkCa 15 (Figure 6). Huang et al. (2017) report an inner hole in the MWC 480 DCO^+ emission, but we do not have the spatial resolution to confirm such a feature. The DCO^+ radial profile around LkCa 15 is suggestive of a double-ring morphology similar to that seen in N_2H+.

DCN is detected toward both disks with emission toward LkCa 15 being 4.1× stronger (Figure 6), consistent with the flux ratio of ∼4 reported in Huang et al. (2017). Similar emission profiles are also observed, with emission in MWC 480 being more centrally peaked and compact, and emission in LkCa 15 containing a central peak and an outer ring.

We additionally report the first detection of DNC in a protoplanetary disk, with strong emission detected around LkCa 15 (Figure 6). The emission appears to have a double-ring morphology similar to DCN and DCO^+. In contrast to these two species, however, the ratio of the outer ring surface brightness to the inner ring surface brightness is considerably higher for DNC. A similar difference in the emission morphologies of HCN and HNC has been observed in the TW Hya and HD 163296 disks (Graninger et al. 2015).

4.5. Sulfur-bearing Species: CS, $C^{34}S$, ^{13}CS, and H_2CS

CS 6–5 emission is strongly detected toward both disks (Figure 7), but is brighter toward LkCa 15 (flux ratio of ∼1.8; 1497 ± 19 versus 811 ± 19 mJy km s^{-1}, respectively), with both the ^{13}CS and $C^{34}S$ isotopologues additionally detected toward LkCa 15. The emission morphology of all CS isotopologues in both disks is compact, but the main isotopologues shows a small dip in the emission center toward MWC 480, similar to the CS emission distribution toward TW Hya (Teague et al. 2017). The central dip in CS emission toward LkCa 15 can likely be explained by its large gas and dust cavity (∼45 au in CO Jin et al. 2019).

In addition to the CS isotopologues, three lines of H_2CS (8_{17}–7_{16}, 9_{19}–8_{18}, and 9_{18}–8_{17}) are detected toward MWC 480 with a very compact emission distribution. No emission is detected toward LkCa 15 above a 4σ level. The S/N of the image plane detection in MWC 480 is quite low, but the stacked filter response is $>8\sigma$. We briefly discuss the formation chemistry of H_2CS in Section 5 as well as in Le Gal et al. (2019), along with possible explanations for why it is detected in MWC 480 and not in LkCa 15.

4.6. Hydrocarbons: $c\text{-}C_3H_2$ and C_2D

Numerous transitions of the hydrocarbon ring $c\text{-}C_3H_2$ are detected around both disks, with emission being much stronger toward MWC 480 (Figure 8). This species has previously been reported in abundance toward both HD 163296 (Qi et al. 2013c) and TW Hya (Bergin et al. 2016), where the emission had clear ringed distributions. Our spatial resolution is too low to resolve the $c\text{-}C_3H_2$ radial distribution, but the MWC 480 radial profile hints at a ring.

Emission rings have also been observed for the hydrocarbon C_2H (Kastner et al. 2015; Bergin et al. 2016), although more varied emission morphologies have recently been observed in other disks (Cleeves et al. 2018; Bergner et al. 2019). C_2H was included in our original survey plan, but unfortunately all transitions were within the unobserved spectral setting. We do, however, detect its deuterated isotopologues C_2D toward MWC 480 (Figure 8). Once again, our spatial resolution is too low to determine a detailed emission profile, but the detection of this deuterated hydrocarbon presents the opportunity for future comparative analysis with other deuterated molecular tracers such as DCN and DCO^+. The filter with the highest response to the C_2D line is DCO^+, tentatively suggesting that they have similar morphologies.

4.7. Nitriles: HC_3N and CH_3CN

Similar to the hydrocarbon species, the nitriles HC_3N and CH_3CN are detected in MWC 480 but not in LkCa 15, although there may be a marginal detection of HC_3N toward LkCa 15 (Figure 9). The emission is spatially compact for both species. These data are presented and discussed in Bergner et al. (2018) in the context of a larger survey of HC_3N and CH_3CN in protoplanetary disks.

5. Discussion

5.1. Comparative Analysis

To compare the molecular inventories of MWC 480 and LkCa 15, we plot integrated flux density ratios in Figure 10. Emission is coupled to excitation temperature, column density, and spatial extent, so without multiple transitions to constrain excitation temperatures, we cannot directly compare abundances between the two disks. With the exception of CS and N_2H^+ though, emission from the species we detect is likely optically thin, suggesting that integrated emission will be roughly proportional to column density, with some multiplicative offset due to the differing excitation conditions of the sources. We therefore use the flux density ratios as a rough proxy for abundance comparisons between the two sources.

5.1.1. $^{13}C^{18}O$, N_2H^+ and H_2CO

Strong $^{13}C^{18}O$ emission is detected toward MWC 480 with none detected toward LkCa 15. Our limits on $^{13}C^{18}O$ in LkCa 15, yielding a lower limit flux ratio of 5.3, are roughly consistent with the $C^{18}O$ flux ratio of ∼6 in the observations used as template filters (see Section 3.2). These results suggest a more massive gas-phase reservoir of CO in MWC 480. This is not surprising, given both that MWC 480 is a more massive disk and that CO is likely frozen out in much of the cold LkCa 15 disk, while it will remain in the gas phase in the warmer MWC 480 disk. CO freeze-out and processing on grains via sequential hydrogenation (e.g., Qi et al. 2013a) can also explain the much higher fluxes of N_2H^+ and H_2CO in LkCa 15. These data are further analyzed in C. Qi et al. (2020, in preparation).

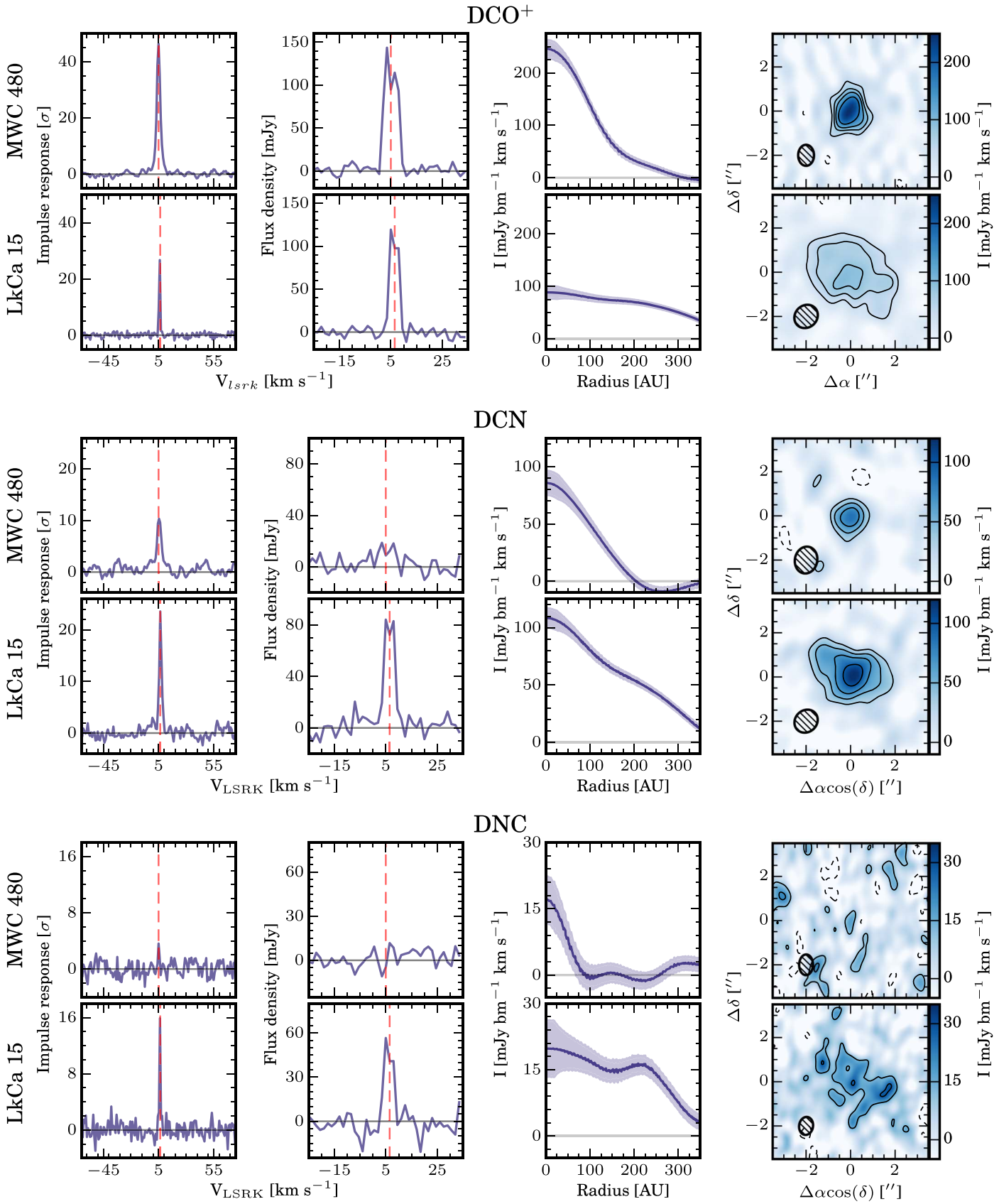

Figure 6. DCO^+, DCN, and DNC observations in MWC 480 and LkCa 15. Panel descriptions are identical to Figure 4, but contours for DNC are $[-2, 2, 4, 6, 8, \ldots] \times \sigma$.

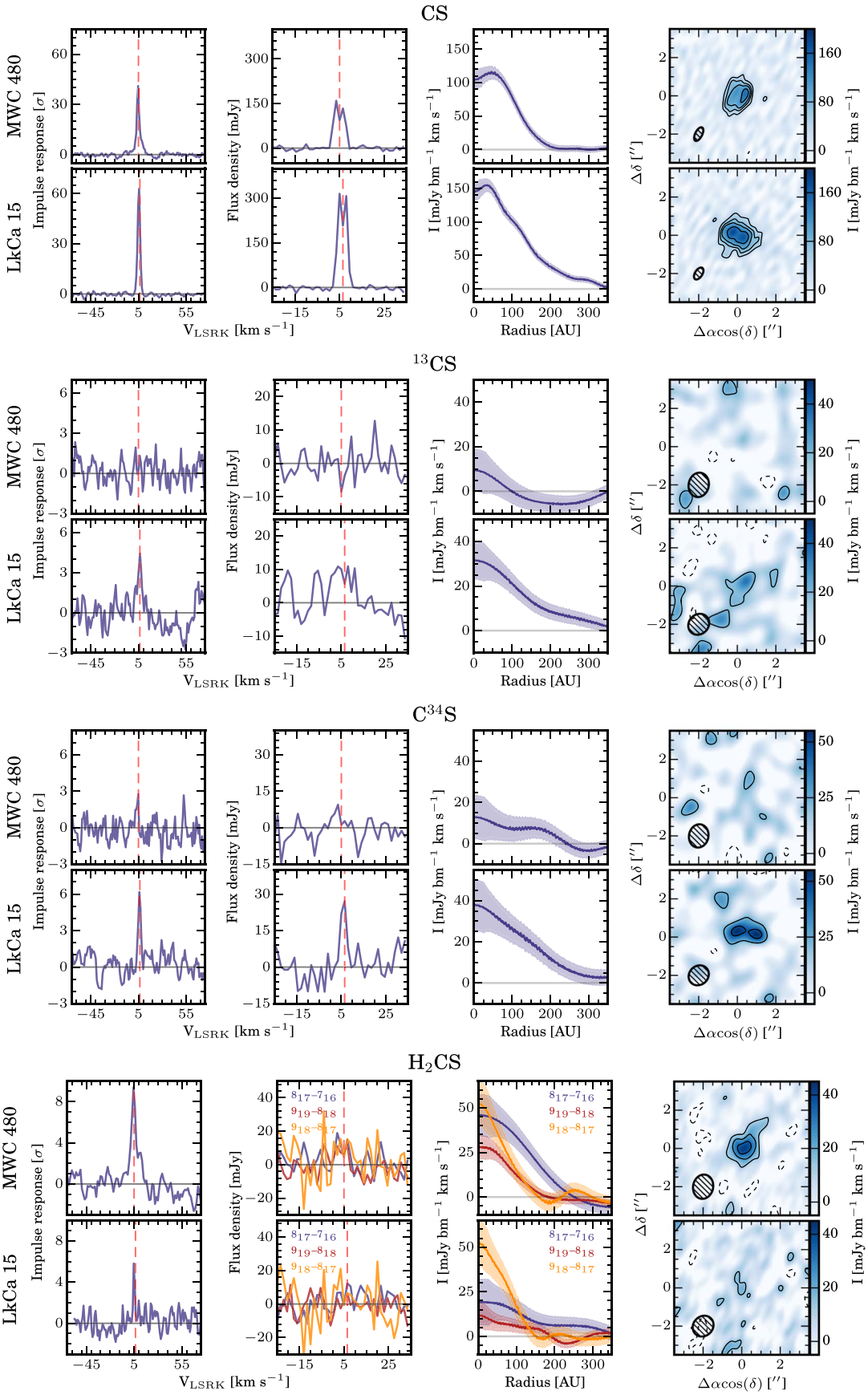

Figure 7. CS, C^{34}S, ^{13}CS, and H$_2$CS observations in MWC 480 and LkCa 15. Panel descriptions are identical to Figure 4, but C^{34}S, ^{13}CS, and H$_2$CS have contours of $[-2, 2, 4, 6, 8, \ldots] \times \sigma$.

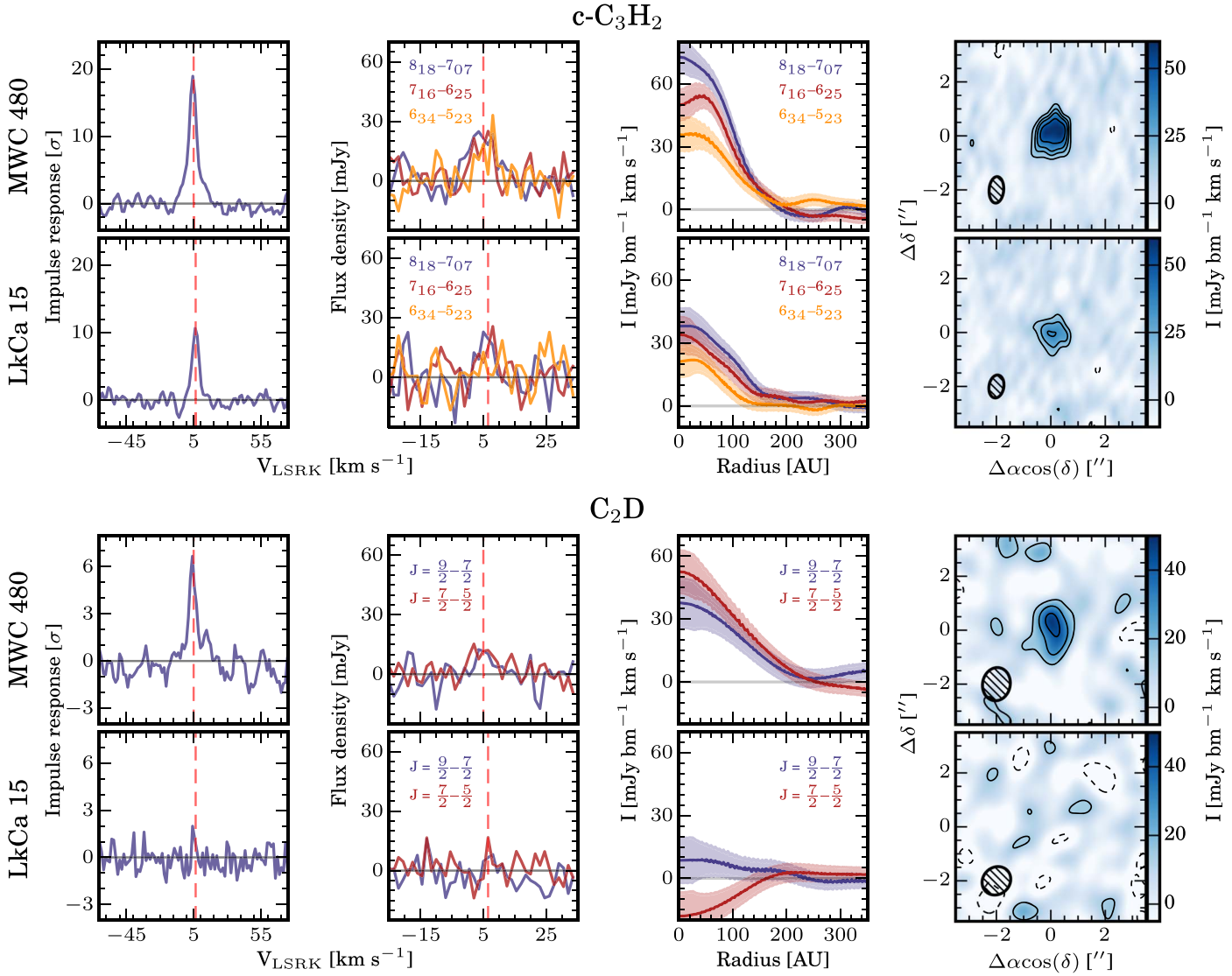

Figure 8. c-C_3H_2 and C_2D observations in MWC 480 and LkCa 15. Panel descriptions are identical to Figure 4, but contours for C_2D are $[-2, 2, 4, 6, 8, \ldots] \times \sigma$.

5.1.2. Deuterated Species

We find that DCO^+ 4–3 emission is much brighter in MWC 480 than in LkCa 15. Huang et al. (2017) find similar integrated flux densities between the two disks, however, for the 3–2 transition of DCO^+. Combining our results with those in Huang et al. (2017) yields a DCO^+ 4–3/3–2 flux ratio of $\sim 1.9 \pm 0.3$ in MWC 480 and $\sim 1.25 \pm 0.3$ in LkCa 15. This may suggest that the DCO^+ in MWC 480 is warmer, which would additionally be consistent with the broad distribution of DCO^+ in LkCa 15 and the more centrally peaked DCO^+ in MWC 480 (i.e., there is more DCO^+ present in the colder outer regions of LkCa 15). The presence of both warm and cold pathways contributing to DCO^+ abundances has also recently been demonstrated in Carney et al. (2018) for the Herbig Ae disk system HD 169142.

Similar to Huang et al. (2017), we also find that the MWC 480/LkCa 15 flux density ratio of DCO^+ is much higher than that of DCN. Huang et al. (2017) interpreted these results as possible evidence that both warm and cold pathways (Roueff et al. 2013) contribute significantly to the formation of DCN. The present detection DNC may offer a possible path for investigating this chemistry further. In the gas phase, DNC forms via reaction of H_2D^+ with HCN, while DCN forms via reaction of H_2D^+ with HNC (e.g., Willacy & Woods 2009). Now that HCN, HNC, DCN, and DNC have all been detected in disks (and three of the four in LkCa 15), future targeted studies may be able to better constrain the chemistry of this small deuteration network.

5.1.3. S-bearing Species

The main CS isotopologues is strongly detected toward both disks and is possibly optically thick at smaller radii (e.g., Teague et al. 2017; Liu et al. 2019), making it difficult to make an abundance comparison from this transition alone. A higher CS column density in LkCa 15 is supported, however, by the fact that the optically thin CS isotopologues ^{13}CS and $C^{34}S$ are only detected there. Emission from the main isotopologues is compact with small emission holes seen for both disks. Observations of CS 5–4 emission toward the edge-on Flying Saucer disk were reported by Dutrey et al. (2017) to be vertically unresolved, suggestive of dominant emission from dense gas near the midplane. If this vertical distribution is also

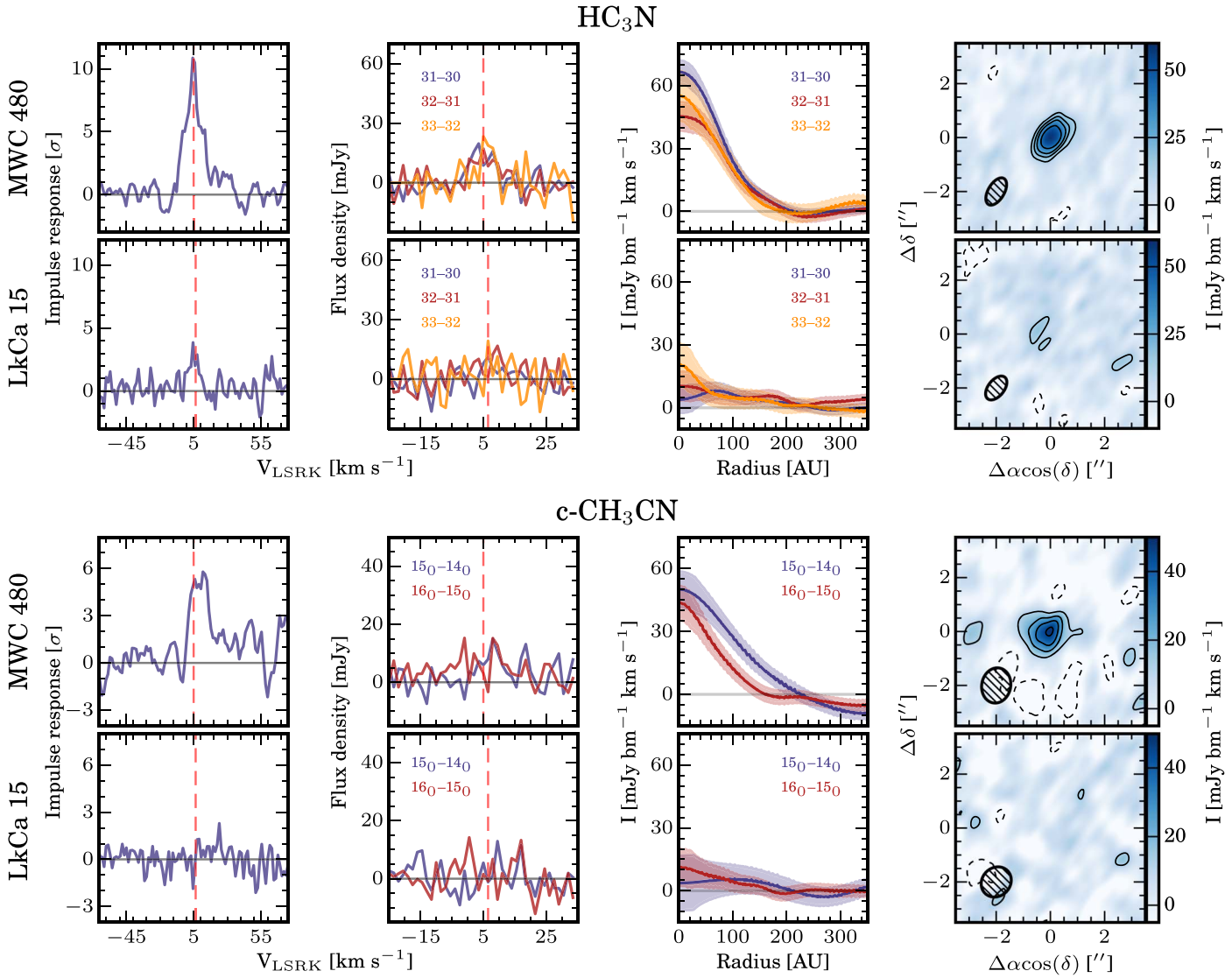

Figure 9. HC_3N and CH_3CN observations in MWC 480 and LkCa 15. Panel descriptions are identical to Figure 4, but with contours of $[-2, 2, 4, 6, 8, \ldots] \times \sigma$.

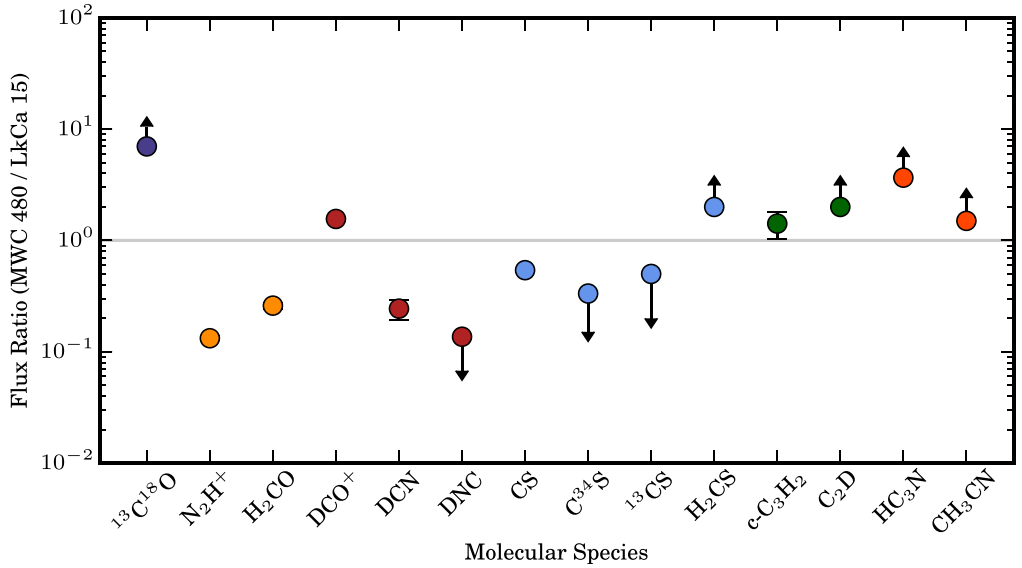

Figure 10. Integrated flux density ratios between MWC 480 and LkCa 15 for each molecule. When a molecule is not detected in one disk, ratio limits are calculated using the 2σ upper limits presented in Table 3. Molecules are color coded by the molecular groups used in Section 4.

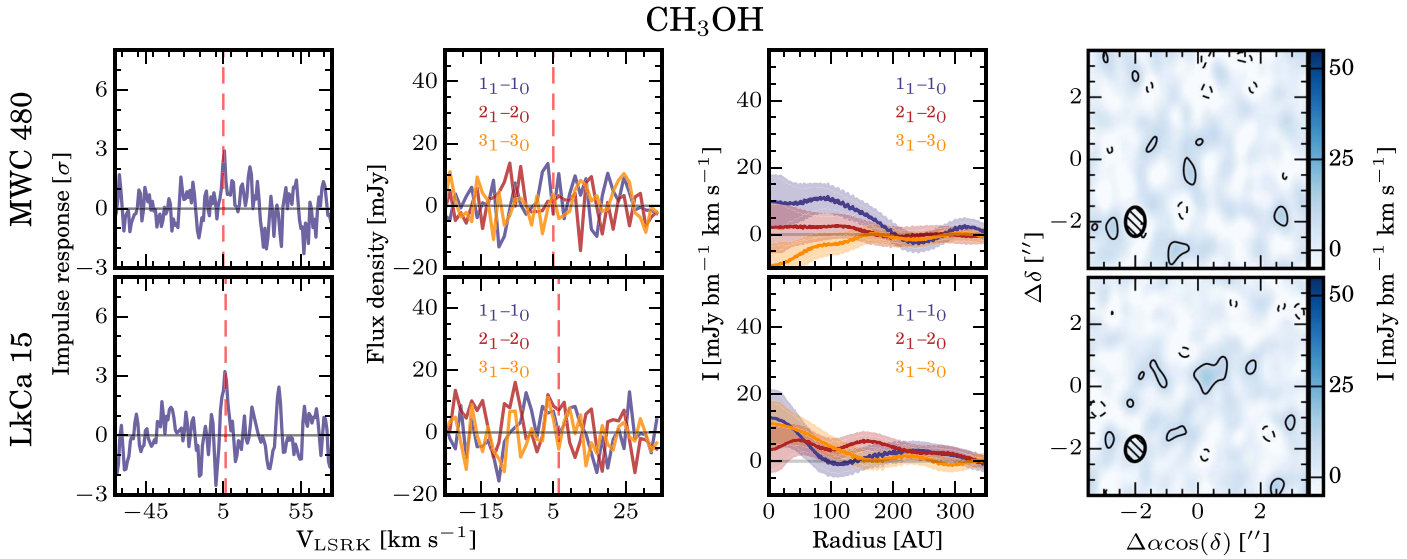

Figure 11. CH_3OH observations in MWC 480 and LkCa 15. Panel descriptions are identical to Figure 4, but with contours of $[-2, 2, 4, 6, 8, \ldots] \times \sigma$.

present in MWC 480, the central depression in the CS emission could be explained by continuum subtraction effects in the inner disk where the dust optical depths are high (e.g., Cleeves et al. 2016; Teague et al. 2017).

Interestingly, H_2CS is detected toward MWC 480 with a compact emission profile, even though we suspect this disk has a lower CS abundance. Unlike its analog H_2CO, H_2CS formation is thought to be dominated by the gas-phase reaction of CH_3 with atomic S (Le Gal et al. 2019), so this discrepancy may be due to the warmer conditions and stronger radiation fields in MWC 480 enhancing the concentration of reactants. These observations are analyzed in more detail in the context of a larger survey of S-bearing species in Le Gal et al. (2019).

5.1.4. Hydrocarbons and Nitriles

The hydrocarbons c-C_3H_2 and C_2D as well as the nitriles HC_3N and CH_3CN are found to be brighter toward MWC 480. One possible cause of this would be an enhanced C/O ratio toward MWC 480, which would then result in increased hydrocarbon and nitrile production, as suggested by Du et al. (2015), Bergin et al. (2016), and Cleeves et al. (2018). We caution however that the upper state energies of the c-C_3H_2 and nitrile transitions are quite high (50–200 K), and thus the measured flux densities are likely to be biased by the warmer temperature of MWC 480. Both of these phenomena are discussed in greater detail in Bergner et al. (2018).

5.2. Double-ringed Structures in LkCa 15

N_2H^+, H_2CO, DCO^+, DCN, and DNC all show varying degrees of evidence for possible double-ring structure in LkCa 15, with an inner ring near the edge of the dust cavity and a second ring around 180 au, near the edge of the millimeter dust disk. This feature was previously reported by Huang et al. (2017) for the 3–2 transition of DCN around LkCa 15, as well as transitions of other species around HD 163296 and IM Lup (where a double ring of DCO^+ was first identified by Öberg et al. 2015). Öberg et al. (2015) and Cleeves et al. (2016) suggest that dust evolution may expose the outer disk to increase levels of irradiation, increasing temperatures and allowing CO to return to the gas phase. If this is the case, it may explain why the chemically linked and CO-sensitive species N_2H^+ and H_2CO have double-ring profiles that follow each other closely.

5.3. Where are the COMs?

Predictions from chemical networks such as Walsh et al. (2014) and Furuya & Aikawa (2014) suggest that a number of larger molecular species (e.g., CH_3CN, CH_3OH, HNCO, HCOOH, and CH_3CHO) should have been detectable in our survey (assuming excitation temperatures of 10–40 K). The detection then of only CH_3CN in one disk is therefore quite interesting, and appears to be in agreement with mounting observational evidence for suppressed COM emission in disks (e.g., Carney et al. 2019). Although there is strong evidence for abundant grain surface formation of COM precursors such as H_2CO in protoplanetary disks (Loomis et al. 2015; Carney et al. 2017; Öberg et al. 2017), the sole detection of CH_3OH thus far (Walsh et al. 2016) found a column density up to an order of magnitude lower than expected from models (Furuya & Aikawa 2014; Walsh et al. 2014).

Searching for CH_3OH lines in our data yields no firm detections, as seen in Figure 11. Two tentative features are identified at $\sim 3\sigma$ in the stacked spectra, but require further analysis and/or follow-up observations to be confirmed. Using the integrated flux uncertainties on each line (determined as detailed in Section 3.3) and assuming an excitation temperature of 25 K (Walsh et al. 2016; Carney et al. 2019), we find a 3σ upper limit column density of $\sim 8 \times 10^{12}$ cm^{-2}, below the column densities expected from models (Furuya & Aikawa 2014; Walsh et al. 2014). A more stringent analysis of these upper limits is presented within the context of a larger sample in J. Ilee et al. (2020, in preparation).

These observations suggest that chemical models overproduce gas-phase abundances of O-bearing complex species. As recently discussed in Walsh et al. (2017), there are two plausible explanations. First, the rate coefficients assumed for O-bearing COM formation mechanisms on grain surfaces may be too high, due to e.g., overestimates of the internal radiation fields in disks. In this scenario, COMs may be present in the gas phase, but at reduced abundances, mirroring their reduced ice abundances. The second possibility is that more complex

species are not able to desorb off the grain surfaces in appreciable quantities. Recent studies suggests that larger molecules such as CH_3OH readily fragment when irradiated, and may not be able to efficiently photodesorb intact from grain surfaces (Bertin et al. 2016; Cruz-Diaz et al. 2016), an explanation which has been invoked to explain observed CH_3OH column densities toward TW Hya (Walsh et al. 2017; Ligterink et al. 2018). Future stacking analyses, deeper targeted integrations, or a combination of both are needed to obtain even limited COM inventories in disks, to explore COM/CH_3OH ratios, and CH_3OH and COM radial and vertical distributions. The latter will especially be key to distinguish between reduced-production and reduced-desorption scenarios, as the photodesorption efficiencies of COMs should depend on disk radius and height.

6. Summary

We have presented an overview of an unbiased interferometric spectral line survey toward the protoplanetary disks MWC 480 and LkCa 15. These results can be summarized as follows:

1. 24 transitions of 14 molecular species are detected, with 5 of these species ($C^{34}S$, ^{13}CS, H_2CS, DNC, and C_2D) detected for the first time in a protoplanetary disk.
2. Matched filtering of the survey using prior observations as templates allowed much faster line identification than a traditional imaging approach and improved S/N by factors of ∼2–3.
3. Significant differences are observed in the molecular inventories of MWC 480 and LkCa 15, which may be mostly explained by temperature differences between the disks.
4. Species that require CO freeze-out are enhanced toward LkCa 15, while the detection of $^{13}C^{18}O$ in MWC 480 suggests highly abundant gas-phase CO.
5. S-bearing species are brighter toward LkCa 15, with the exception of H_2CS. Its presence in MWC 480 can likely be explained by warm gas-phase chemistry, which is investigated further in Le Gal et al. (2019).
6. Observed transitions of hydrocarbons and nitriles are brighter toward MWC 480. It is unclear if this is due to the high upper state energies of these transitions and therefore a temperature bias, or whether abundances are truly higher toward MWC 480, suggestive of an enhanced C/O ratio. Forward modeling (beyond the scope of this work) may be able to distinguish between these scenarios.
7. Emission from COMs such as CH_3OH, CH_3CHO, and HCOOH is conspicuously absent, in conflict with column density predictions from chemical models, although two tentative features are found in the stacked CH_3OH spectra. These results are in line with the low CH_3OH column densities observed in TW Hya and discussed in Walsh et al. (2017) and Carney et al. (2019), possibly suggesting that the desorption rates of O-bearing COMs in disk chemical models are currently overestimated.

R.A.L. gratefully acknowledges funding from ALMA Student Observing Support and a Jansky Fellowship. K.I.O. acknowledges funding from the David and Lucile Packard Foundation and from the Simons Foundation (SCOL #321183). J.H. acknowledges support from the National Science Foundation Graduate Research Fellowship under grant No. DGE-1144152. E.A.B. acknowledges funding through NSF grant AST-1514670 and NASA NNX16AB48G. C.W. acknowledges financial support from STFC (grant reference ST/R000549/1) and the University of Leeds. The National Radio Astronomy Observatory is a facility of the National Science Foundation operated under cooperative agreement by Associated Universities, Inc. This paper makes use of the following ALMA data: ADS/JAO.ALMA#2013.1.00226.S and ADS/JAO.ALMA#2015.1.00657.S. ALMA is a partnership of ESO (representing its member states), NSF (USA) and NINS (Japan), together with NRC (Canada) and NSC and ASIAA (Taiwan), in cooperation with the Republic of Chile. The Joint ALMA Observatory is operated by ESO, AUI/NRAO, and NAOJ.

ORCID iDs

Ryan A. Loomis https://orcid.org/0000-0002-8932-1219
Karin I. Öberg https://orcid.org/0000-0001-8798-1347
Sean M. Andrews https://orcid.org/0000-0003-2253-2270
Edwin Bergin https://orcid.org/0000-0003-4179-6394
Jennifer Bergner https://orcid.org/0000-0002-8716-0482
Geoffrey A. Blake https://orcid.org/0000-0003-0787-1610
L. Ilsedore Cleeves https://orcid.org/0000-0003-2076-8001
Ian Czekala https://orcid.org/0000-0002-1483-8811
Jane Huang https://orcid.org/0000-0001-6947-6072
Romane Le Gal https://orcid.org/0000-0003-1837-3772
Francois Ménard https://orcid.org/0000-0002-1637-7393
Jamila Pegues https://orcid.org/0000-0002-6042-1486
Chunhua Qi https://orcid.org/0000-0001-8642-1786
Catherine Walsh https://orcid.org/0000-0001-6078-786X
Jonathan P. Williams https://orcid.org/0000-0001-5058-695X
David J. Wilner https://orcid.org/0000-0003-1526-7587

References

Andrews, S. M., Rosenfeld, K. A., Kraus, A. L., & Wilner, D. J. 2013, ApJ, 771, 129
Belloche, A., Garrod, R. T., Müller, H. S. P., et al. 2009, A&A, 499, 215
Belloche, A., Menten, K. M., Comito, C., et al. 2008a, A&A, 482, 179
Belloche, A., Menten, K. M., Comito, C., et al. 2008b, A&A, 482, 179
Belloche, A., Meshcheryakov, A. A., Garrod, R. T., et al. 2017, A&A, 601, A49
Bennett, C. J., & Kaiser, R. I. 2007, ApJ, 661, 899
Bergin, E. A., Du, F., Cleeves, L. I., et al. 2016, ApJ, 831, 101
Bergner, J. B., Guzman, V. G., Öberg, K. I., Loomis, R. A., & Pegues, J. 2018, ApJ, 857, 69
Bergner, J. B., Öberg, K. I., Bergin, E. A., et al. 2019, ApJ, 876, 25
Bertin, M., Romanzin, C., Doronin, M., et al. 2016, ApJL, 817, L12
Blake, G. A., Sutton, E. C., Masson, C. R., & Phillips, T. G. 1986, ApJS, 60, 357
Blake, G. A., van Dishoeck, E. F., Jansen, D. J., Groesbeck, T. D., & Mundy, L. G. 1994, ApJ, 428, 680
Booth, A. S., Walsh, C., Kama, M., et al. 2018, A&A, 611, A16
Carney, M. T., Fedele, D., Hogerheijde, M. R., et al. 2018, A&A, 614, A106
Carney, M. T., Hogerheijde, M. R., Guzmán, V. V., et al. 2019, A&A, 623, A124
Carney, M. T., Hogerheijde, M. R., Loomis, R. A., et al. 2017, A&A, 605, A21
Chiang, E. I., Joung, M. K., Creech-Eakman, M. J., et al. 2001, ApJ, 547, 1077
Cleeves, L. I., Bergin, E. A., Qi, C., Adams, F. C., & Öberg, K. I. 2015, ApJ, 799, 204
Cleeves, L. I., Öberg, K. I., Wilner, D. J., et al. 2016, ApJ, 832, 110
Cleeves, L. I., Öberg, K. I., Wilner, D. J., et al. 2018, ApJ, 865, 155
Cruz-Diaz, G. A., Martín-Doménech, R., Muñoz Caro, G. M., & Chen, Y.-J. 2016, A&A, 592, A68
Czekala, I., Andrews, S. M., Jensen, E. L. N., et al. 2015, ApJ, 806, 154
Du, F., Bergin, E. A., & Hogerheijde, M. R. 2015, ApJL, 807, L32

Dutrey, A., Guilloteau, S., Piétu, V., et al. 2017, A&A, 607, A130
Dutrey, A., Henning, T., Guilloteau, S., et al. 2007, A&A, 464, 615
Favre, C., Fedele, D., Semenov, D., et al. 2018, ApJL, 862, L2
Flaherty, K. M., Hughes, A. M., Teague, R., et al. 2018, ApJ, 856, 117
Fuchs, G. W., Cuppen, H. M., Ioppolo, S., et al. 2009, A&A, 505, 629
Furuya, K., & Aikawa, Y. 2014, ApJ, 790, 97
Gaia Collaboration, Brown, A. G. A., Vallenari, A., et al. 2018, A&A, 616, A1
Garrod, R. T., Weaver, S. L. W., & Herbst, E. 2008, ApJ, 682, 283
Graninger, D., Öberg, K. I., Qi, C., & Kastner, J. 2015, ApJL, 807, L15
Guilloteau, S., Simon, M., Piétu, V., et al. 2014, A&A, 567, A117
Guzmán, V. V., Öberg, K. I., Huang, J., Loomis, R., & Qi, C. 2017, ApJ, 836, 30
Helling, C., Woitke, P., Rimmer, P. B., et al. 2014, Life, 4, 142
Herbig, G. H., & Bell, K. R. 1988, Third Catalog of Emission-Line Stars of the Orion Population:3:1988 (Santa Cruz, CA: Lick Observatory)
Huang, J., Öberg, K. I., Qi, C., et al. 2017, ApJ, 835, 231
Isella, A., Pérez, L. M., & Carpenter, J. M. 2012, ApJ, 747, 136
Jin, S., Isella, A., Huang, P., et al. 2019, ApJ, 881, 108
Johansson, L. E. B., Andersson, C., Ellder, J., et al. 1984, A&A, 130, 227
Jørgensen, J. K., van der Wiel, M. H. D., Coutens, A., et al. 2016, A&A, 595, A117
Kaifu, N., Ohishi, M., Kawaguchi, K., et al. 2004, PASJ, 56, 69
Kastner, J. H., Hily-Blant, P., Rodriguez, D. R., Punzi, K., & Forveille, T. 2014, ApJ, 793, 55
Kastner, J. H., Qi, C., Dickson-Vandervelde, D. A., et al. 2018, ApJ, 863, 106
Kastner, J. H., Qi, C., Gorti, U., et al. 2015, ApJ, 806, 75
Le Gal, R., Öberg, K. I., Loomis, R. A., Pegues, J., & Bergner, J. B. 2019, ApJ, 876, 72
Ligterink, N. F. W., Walsh, C., Bhuin, R. G., et al. 2018, A&A, 612, A88
Liu, Y., Dipierro, G., Ragusa, E., et al. 2019, A&A, 622, A75
Loomis, R., Öberg, K., Andrews, S., et al. 2018a, VISIBLE: VISIbility Based Line Extraction, Astrophysics Source Code Library, ascl:1802.006
Loomis, R. A., Cleeves, L. I., Öberg, K. I., et al. 2018b, ApJ, 859, 131
Loomis, R. A., Cleeves, L. I., Öberg, K. I., Guzman, V. V., & Andrews, S. M. 2015, ApJL, 809, L25
Loomis, R. A., Öberg, K. I., Andrews, S. M., et al. 2018c, AJ, 155, 182
Loomis, R. A., Zaleski, D. P., Steber, A. L., et al. 2013, ApJL, 765, L9
Luhman, K. L., Allen, P. R., Espaillat, C., Hartmann, L., & Calvet, N. 2010, ApJS, 186, 111
Mannings, V., & Sargent, A. I. 1997, ApJ, 490, 792
McGuire, B. A. 2018, ApJS, 239, 17
McGuire, B. A., Carroll, P. B., Loomis, R. A., et al. 2016, Sci, 352, 1449
McGuire, B. A., Loomis, R. A., Charness, C. M., et al. 2012, ApJL, 758, L33
Miotello, A., van Dishoeck, E. F., Kama, M., & Bruderer, S. 2016, A&A, 594, A85
Miotello, A., van Dishoeck, E. F., Williams, J. P., et al. 2017, A&A, 599, A113
North, D. O. 1963, IEEEP, 51, 1016
Öberg, K. I., Garrod, R. T., van Dishoeck, E. F., & Linnartz, H. 2009, A&A, 504, 891
Öberg, K. I., Guzmán, V. V., Furuya, K., et al. 2015, Natur, 520, 198
Öberg, K. I., Guzmán, V. V., Merchantz, C. J., et al. 2017, ApJ, 839, 43
Öberg, K. I., Qi, C., Fogel, J. K. J., et al. 2010, ApJ, 720, 480
Öberg, K. I., Qi, C., Fogel, J. K. J., et al. 2011, ApJ, 734, 98
Ossenkopf, V., Müller, H. S. P., Lis, D. C., et al. 2010, A&A, 518, L111
Pegues, J., Öberg, K. I., & Bergner, J. B. 2020, ApJ, 890, 142
Pety, J., Gratier, P., Guzmán, V., et al. 2012, A&A, 548, A68
Phuong, N. T., Chapillon, E., Majumdar, L., et al. 2018, A&A, 616, L5
Piétu, V., Dutrey, A., & Guilloteau, S. 2007, A&A, 467, 163
Pinte, C., Ménard, F., Duchêne, G., et al. 2018, A&A, 609, A47
Punzi, K. M., Hily-Blant, P., Kastner, J. H., Sacco, G. G., & Forveille, T. 2015, ApJ, 805, 147
Qi, C., Öberg, K. I., Andrews, S. M., et al. 2015, ApJ, 813, 128
Qi, C., Öberg, K. I., & Wilner, D. J. 2013a, ApJ, 765, 34
Qi, C., Öberg, K. I., Wilner, D. J., et al. 2013b, Sci, 341, 630
Qi, C., Öberg, K. I., Wilner, D. J., & Rosenfeld, K. A. 2013c, ApJL, 765, L14
Remijan, A. J., Hollis, J. M., Jewell, P. R., & Lovas, F. J. 2009, in 64th Int. Symp. Molecular Spectroscopy, TH02
Rosenfeld, K. A., Andrews, S. M., Hughes, A. M., Wilner, D. J., & Qi, C. 2013, ApJ, 774, 16
Rosenfeld, K. A., Qi, C., Andrews, S. M., et al. 2012, ApJ, 757, 129
Roueff, E., Gerin, M., Lis, D. C., et al. 2013, JPCA, 117, 9959
Schwarz, K. R., Bergin, E. A., Cleeves, L. I., et al. 2018, ApJ, 856, 85
Simon, M., Dutrey, A., & Guilloteau, S. 2000, ApJ, 545, 1034
Teague, R., Guilloteau, S., Semenov, D., et al. 2016, A&A, 592, A49
Teague, R., Semenov, D., Gorti, U., et al. 2017, ApJ, 835, 228
The, P. S., de Winter, D., & Perez, M. R. 1994, A&AS, 104, 315
Thi, W.-F., van Zadelhoff, G.-J., & van Dishoeck, E. F. 2004, A&A, 425, 955
van Dishoeck, E. F., Blake, G. A., Jansen, D. J., & Groesbeck, T. D. 1995, ApJ, 447, 760
van't Hoff, M. L. R., Walsh, C., Kama, M., Facchini, S., & van Dishoeck, E. F. 2017, A&A, 599, A101
Walsh, C., Juhász, A., Meeus, G., et al. 2016, ApJ, 831, 200
Walsh, C., Millar, T. J., Nomura, H., et al. 2014, A&A, 563, A33
Walsh, C., Vissapragada, S., & McGee, H. 2017, in IAU Symp. 332, Astrochemistry VII: Through the Cosmos from Galaxies to Planets, ed. M. Cunningham, T. Millar, & Y. Aikawa (Cambridge: Cambridge Univ. Press)
Watanabe, N., & Kouchi, A. 2002, ApJL, 571, L173
Willacy, K., & Woods, P. M. 2009, ApJ, 703, 479
Yu, M., Evans, N. J., II, Dodson-Robinson, S. E., Willacy, K., & Turner, N. J. 2017, ApJ, 841, 39
Zaleski, D. P., Seifert, N. A., Steber, A. L., et al. 2013, ApJL, 765, L10
Zhang, K., Bergin, E. A., Blake, G. A., Cleeves, L. I., & Schwarz, K. R. 2017, NatAs, 1, 0130